


Substrate-induced broken C_4 symmetry and gap variation in superconducting single-layer FeSe/SrTiO₃-($\sqrt{13} \times \sqrt{13}$)

Wen Si (司文),* Tomoaki Tanaka (田中友晃), Satoru Ichinokura (一ノ倉聖), and Toru Hirahara (平原徹)[†]
Department of Physics, Tokyo Institute of Technology, Tokyo 152-8551, Japan

 (Received 24 November 2021; revised 24 January 2022; accepted 16 February 2022; published 1 March 2022)

We performed scanning tunneling microscopy/spectroscopy (STM/STS) measurements to investigate the superconducting properties of single-layer FeSe grown on SrTiO₃ (STO) (001)-($\sqrt{13} \times \sqrt{13}$). We found “+” and “z” patterns arranged in $\sqrt{13} \times \sqrt{13}$ periodicity in the STM images. Surprisingly, they show C_2 symmetry, although free-standing FeSe itself has C_4 symmetry. STS spectra and quasiparticle interference patterns near the Fermi level also indicate the broken C_4 symmetry with the superconducting gap showing a local variation within the STO surface unit cell because of the short coherence length. This clearly shows the non-negligible role of the substrate surface in the superconductivity of the FeSe/STO system.

DOI: [10.1103/PhysRevB.105.104502](https://doi.org/10.1103/PhysRevB.105.104502)

I. INTRODUCTION

The superconducting transition temperature (T_C) in single-layer one unit cell (1-UC) FeSe grown on SrTiO₃ (STO) (001) is over 40 K [1–3], while it is only 8 K for bulk FeSe [4]. Although it is still debated which mechanism enhances the T_C , the STO substrate is undoubtedly responsible. Intensive research has been performed in terms of the STO substrate-induced electron doping [5–9] or electron-phonon coupling [10–13]. We have previously shown that the difference in the STO surface periodicity [2×1 , $\sqrt{2} \times \sqrt{2}$, and $c(6 \times 2)$] can modulate the superconductivity of 1-UC FeSe since the difference in the Ti and O configurations at the surface can change the electron doping [14–19].

Another important aspect of the 1-UC FeSe/STO system is the short coherent length. In Ref. [20], the Pippard coherence length of 1-UC FeSe/STO was calculated to be 1.2 nm from the band structure. In another work, the Ginzburg-Landau coherence length was estimated as 2.85 nm from the vortex observation [21]. The arrangement of O vacancies within the STO surface unit cell can lead to a local inhomogeneity in the electron doping. This variation can be experimentally probed since the coherence length is in the same order of magnitude as the unit cell size (1–2 nm) by examining the local superconducting gap difference, similar to the case of Bi₂Sr₂CaCu₂O_{8-x} (BSCCO)[22]. However, such a local difference in the pair coupling strength in this system has yet to be clarified.

Therefore, we aimed to investigate the local superconducting properties of 1-UC FeSe grown on the STO-($\sqrt{13} \times \sqrt{13}$), which has a unit cell as large as 1.4×1.4 nm². From scanning tunneling microscopy/spectroscopy (STM/STS) measurements, we observed “+” and “z” patterns under different biases arranged in the $\sqrt{13} \times \sqrt{13}$ periodicity and

found that the C_4 symmetry of the 1-UC FeSe is broken. Atom-resolved STS measurements clearly showed that the local tunneling conductance (dI/dV) and the superconducting gap size are different within the $\sqrt{13} \times \sqrt{13}$ unit cell. Furthermore, we found that the quasiparticle interference (QPI) images also showed broken C_4 symmetry. The obtained band structure from the QPI measurement was consistent with that measured with angle-resolved photoemission spectroscopy (ARPES). We conclude that the C_2 symmetry of the STO-($\sqrt{13} \times \sqrt{13}$) surface is responsible for the observed broken C_4 symmetry of FeSe.

II. EXPERIMENTAL DETAILS

A commercially available Nb-doped SrTiO₃(001) (0.5 wt %, Shinkosha) was used as the substrate. After degassing at 500 °C in ultrahigh vacuum for 3 h, the samples were annealed in an oxygen atmosphere ($P_{O_2} = 1 \times 10^{-5}$ Torr) to obtain double TiO_x-terminated $\sqrt{13} \times \sqrt{13}$ surface reconstruction [19]. Following a 1.5-h annealing at 850 °C and a 30-min annealing at 950 °C, we observed a strong $\sqrt{13} \times \sqrt{13}$ reflection high-energy electron diffraction (RHEED) pattern.

The 1-UC FeSe was formed by codepositing Fe (99.5%) and Se (99.999%) with a flux ratio of 1 : 10 (Se rich) on the $\sqrt{13} \times \sqrt{13}$ surface with the substrate temperature kept at 400 °C. The growth process was monitored with RHEED and the intensity oscillation was used to determine the film thickness.

In situ STM/STS (Unisoku USM1500) measurements were performed at 5 K with PtIr tips. A standard lock-in technique was used in the tunneling conductance (dI/dV) measurements with bias modulations of 1 mV for $V_{set} \leq 100$ mV and 10 mV for $V_{set} = 1.0$ V. The modulation frequency was set to $f = 1.093$ kHz.

In situ ARPES experiments were performed at 26 K with a hemispherical analyzer equipped with energy and angle

*tsukasa@surfnano.phys.titech.ac.jp

†hirahara@phys.titech.ac.jp

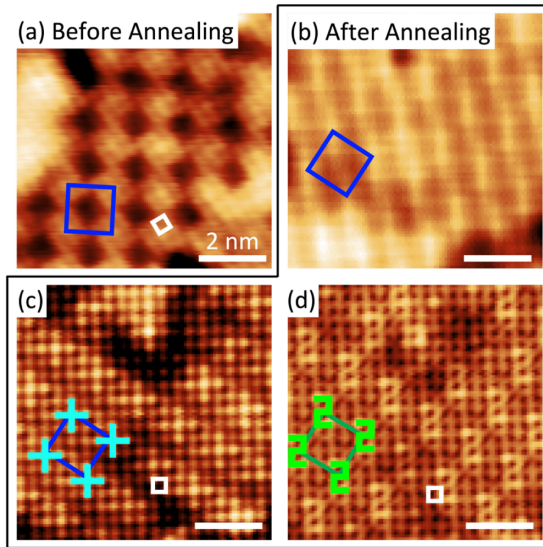


FIG. 1. STM topographic images of the as-deposited 1-UC FeSe/STO- $(\sqrt{13} \times \sqrt{13})$: (a) Before annealing, and (b)–(d) those after sufficient annealing ($7.5 \times 7.5 \text{ nm}^2$). White and dark blue/green squares indicate 1×1 and $\sqrt{13} \times \sqrt{13}$ periodicity, respectively. In (c) and (d), both light blue + and green z patterns are arranged in a $\sqrt{13} \times \sqrt{13}$ periodicity. Set points: (a), (b) 1.0 V, 300 pA; (c) 100 mV, 100 pA; (d) 50 mV, 100 pA.

multidetections (ScientaOmicron R4000) with He 1α radiation (21.2 eV).

III. RESULTS

Figure 1 shows the typical topographic images of 1-UC FeSe grown on STO- $\sqrt{13} \times \sqrt{13}$. The feature in Fig. 1(a) usually appears on the as-deposited samples or films that have been annealed at low temperature ($T_{\text{anneal}} \leq 450^\circ\text{C}$). The length of the white square is $a_{\text{Se}} \approx 3.9 \text{ \AA}$, which coincides with the topmost Se-Se distance of 1-UC FeSe/STO. Considering that the area of the blue square is 13 times as large as the 1×1 unit cell and rotated by 33.7° , we can say that the $\sqrt{13} \times \sqrt{13}$ surface reconstruction of the STO substrates is observed through the FeSe film. After sufficient annealing ($480\text{--}550^\circ\text{C}$ for 30 min), stripelike patterns arranged in a $\sqrt{13} \times \sqrt{13}$ period become dominant as shown in Fig. 1(b), while the 1×1 unit cell becomes invisible at the same set point. We acquired atomically resolved topographic images of the sufficiently annealed sample by changing the set point as shown in Figs. 1(c) and 1(d). One can say that the $\sqrt{13} \times \sqrt{13}$ periodicity exhibits a clear bias dependence. For $V_{\text{set}} = 100 \text{ mV}$, “+” patterns can be recognized while “z” patterns emerge noticeably in the same region when $V_{\text{set}} = 50 \text{ mV}$. Figures 2(a) and 2(b) show the enlarged atom-resolved topographic images of the $\sqrt{13} \times \sqrt{13}$ periodicity of the 1-UC FeSe/STO at $V_{\text{set}} = 80$ and 60 mV , respectively. By referring to an impurity atom marked by the circle, we were able to determine the relative position between the + and z patterns. Namely, they are shifted by half a unit cell along z direction. It should be emphasized that due to the twofold rotational symmetry of the z pattern, the C_4 symmetry of the free-standing 1-UC FeSe is broken and the 1-UC

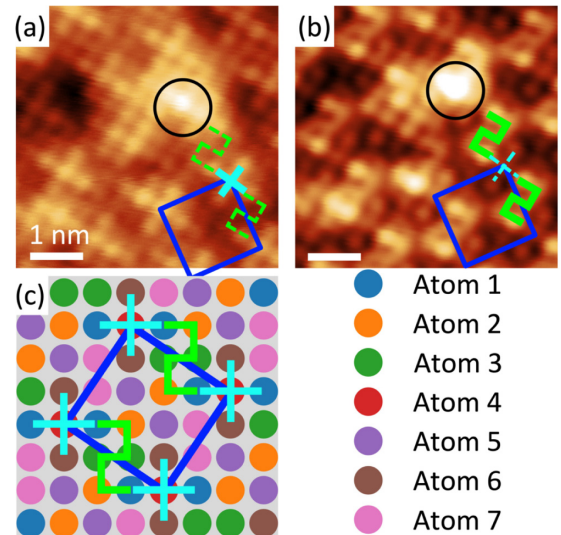


FIG. 2. (a), (b) Atom-resolved topographic images of sufficiently annealed 1-UC FeSe/STO in the same area ($5 \times 5 \text{ nm}^2$). Set points: (a) 80 mV, 100 pA; (b) 60 mV, 100 pA. Impurity atom marked by a black circle helps determine the relation between the + pattern in (a) and the z patterns in (b). The dashed z pattern and + pattern illustrate the relative position of + and z. (c) Schematic image of $\sqrt{13} \times \sqrt{13}$ unit cell (dark blue square) with C_2 symmetry; solid circles with different colors represent seven inequivalent Se sites; + and z patterns are also marked out. Dark blue squares show the same $\sqrt{13} \times \sqrt{13}$ unit cell.

FeSe/STO- $\sqrt{13} \times \sqrt{13}$ only possesses C_2 symmetry. Taking this C_2 symmetry into account, we can classify the topmost Se atoms in the $\sqrt{13} \times \sqrt{13}$ unit cell to seven inequivalent atoms as shown in the schematic image of Fig. 2(c). The solid circles shown in seven different colors represent the inequivalent atoms. Atoms that form the + and z patterns are marked: atoms 1, 4, and 6 form the +, while atoms 1, 2, and 3 form the z pattern. Dark blue squares in Fig. 2 show the same $\sqrt{13} \times \sqrt{13}$ unit cell. Taking the center atom of the + pattern (atom 4) as the corner of the $\sqrt{13} \times \sqrt{13}$ unit cell, the z patterns should locate on one pair of edges of the square unit cell.

Next we measured the dI/dV spectra above all seven inequivalent atoms in the $\sqrt{13} \times \sqrt{13}$ unit cell to determine whether the C_2 symmetry affects the superconductivity properties of 1-UC FeSe. Figure 3(a) shows the averaged dI/dV spectra, indicating a clear local dI/dV difference among different atomic sites. Especially around $\pm 40 \text{ mV}$ and the quasiparticle peak positions, which correspond to the size of the superconducting gap (Δ), a tremendous amount of difference in the local density of states (LDOS) can be found. In Fig. 3(b), zoom-ins of the averaged spectra at the occupied states are shown. The peak position (Δ_{avg}) is derived by Lorentzian fitting combined with linear backgrounds [23], and the results are summarized in Table I. Furthermore, we show the statistical analysis of Δ for all inequivalent atoms in the $\sqrt{13} \times \sqrt{13}$ unit cell in Fig. 3(c). We used 330 spectra distributed in four adjacent $\sqrt{13} \times \sqrt{13}$ unit cells, and the measurements were performed for nearly the same times for each inequivalent atom. We have fitted this distribution with a Gaussian function and deduced the gap size Δ_{stat} ,

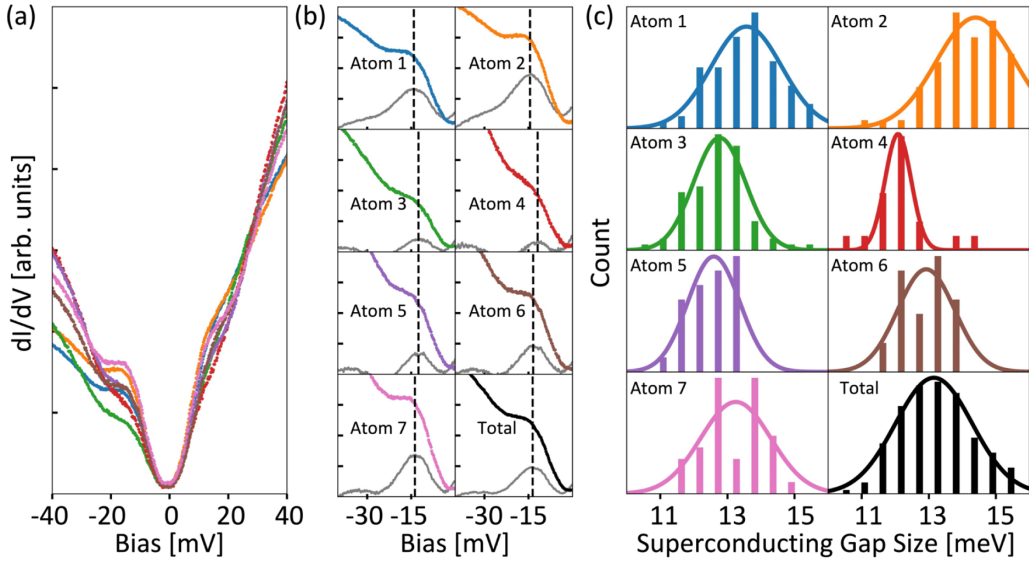


FIG. 3. (a), (b) The dI/dV spectra obtained on top of all seven inequivalent Se atoms. (Set point: 42 mV, 100 pA.) All spectra are averaged on the corresponding Se atom. The spectra colors and relative measuring positions correspond to the schematic image in Fig. 2(c). (a) Spectra aligned without offset, indicating the local dI/dV difference from -40 to 40 mV. (b) Zoom-in spectra aligned with the linear-background-subtracted spectra (gray curves) for the occupied states; dashed lines show peak differences among different atoms. (c) Statistics of the superconducting gap size Δ extracted from spectra taken on all seven inequivalent Se atoms. Totals in (b) and (c) show the average and the distribution of all the measured 330 spectra, respectively.

which is also summarized in Table I. For both Δ_{avg} and Δ_{stat} , there is a sizable difference between the superconducting gap size between atoms 2 and 4. Namely, Δ is 14 and 12 meV, respectively. Thus, this unambiguously shows that the superconducting gap size is locally different in 1-UC FeSe/STO- $(\sqrt{13} \times \sqrt{13})$.

The above observation clearly shows the local inhomogeneity in the dI/dV spectra within the STO surface $\sqrt{13} \times \sqrt{13}$ unit cell. To verify whether the broken C_4 symmetry in the local spectra can be observed nonlocally, e.g., in the band dispersion or electron scattering, we measured the tunneling conductance map $dI/dV(\mathbf{r}, \text{eV})$ of the 1-UC FeSe/STO- $(\sqrt{13} \times \sqrt{13})$ region with defects. Figures 4(a) and 4(b) display the QPI patterns at 17 and -58 mV, respectively. In Fig. 4(a), the standing wave feature is clearly observed, while it seems that the wave feature is prominent for one direction in Fig. 4(b). This also seems to indicate the loss of C_4 symmetry. To investigate the evolution of the QPI patterns, we performed tunneling conductance mapping at several set points and made a fast Fourier transform (FFT) analysis. Figures 4(c)–4(f) present FFT of the tunneling conductance map at the corresponding set points. We observed nine ringlike patterns, centered at the reciprocal lattice point $\mathbf{G} = (0, 0)$, $(\pm 2\pi/a_{\text{Se}}, 0)$,

$(0, \pm 2\pi/a_{\text{Se}})$, and $(\pm 2\pi/a_{\text{Se}}, \pm 2\pi/a_{\text{Se}})$, respectively. These rings originate from intraband and interband scattering of the electron band at the M point [24]. One can notice that the intensities of the rings at $\mathbf{G} = (-2\pi/a_{\text{Se}}, +2\pi/a_{\text{Se}})$ and $(+2\pi/a_{\text{Se}}, +2\pi/a_{\text{Se}})$ are different (solid red and dashed blue circles, respectively), and especially for Figs. 4(c) and 4(f), the blue circles almost disappear. This clearly indicates that C_4 symmetry is also broken in the QPI phenomena [25].

We then applied Lorentzian peak fitting to the azimuthally averaged intensity plot of the QPI patterns as shown in Fig. 4(g) to determine the radius of these rings, which is a similar process to the analysis shown in Ref. [26]. The red circles in Figs. 4(c)–4(e) also represent the results of the above analysis, revealing the norm of the scattering vector \mathbf{q} . The situation in Fig. 4(f) is not so clear due to the broad distribution of the intensity plot. Since the derived \mathbf{q} vector corresponds to that of the intraband scattering [24], we are able to deduce the band dispersion of the electron pocket at the M point near the Fermi level. Figure 4(h) shows the band dispersion obtained from the QPI patterns. They can be fitted by a parabola. Shown together is the band image obtained from ARPES. The bands determined separately by STM/STS and ARPES measurements show excellent agreement and thus one can be sure that the present QPI mapping is showing

TABLE I. Gap size in meV extracted from Fig. 3 for the inequivalent atoms in the $\sqrt{13} \times \sqrt{13}$ unit cell. Δ_{avg} shows the gap size of the averaged spectra in Fig. 3(b). The errors show the error of the Lorentzian fitting. Δ_{stat} shows the gap size extracted from the distribution of gap size in Fig. 3(c). The error of the Δ_{stat} is the standard deviation of the Gaussian distribution. Bold numbers are set to emphasize the significant differences of superconducting gap size between atoms 2 and 4.

Atom index	1	2	3	4	5	6	7	Total
Δ_{avg} (meV)	14.06 \pm 0.04	14.47 \pm 0.05	12.50 \pm 0.13	11.89 \pm 0.12	12.49 \pm 0.09	13.38 \pm 0.07	13.73 \pm 0.06	13.56 \pm 0.04
Δ_{stat} (meV)	13.57 \pm 1.05	14.40 \pm 1.17	12.77 \pm 0.77	12.08 \pm 0.39	12.60 \pm 0.77	12.92 \pm 0.85	13.25 \pm 1.04	13.17 \pm 1.17

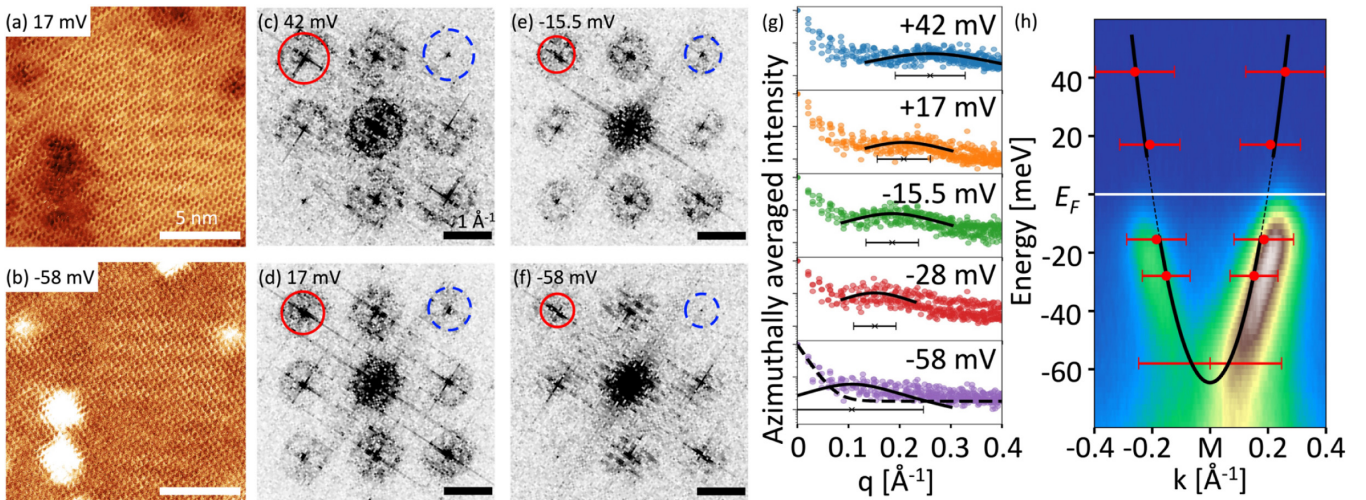


FIG. 4. (a), (b) dI/dV maps measured in the same area ($15 \times 15 \text{ nm}^2$). Biases are (a) 17 mV and (b) -58 mV . Tunneling current is set to 100 pA. (c)–(f) Fast Fourier transform (FFT) of the dI/dV maps at difference biases which correspond to the QPI patterns. Red circles mark the radius of the scattering vector deduced from the peak fitting of the azimuthally averaged intensity of QPI patterns. The dashed blue circles indicate the weakening of the ring intensity. Biases of the corresponding dI/dV maps are (c) 42 mV, (d) 17 mV, (e) -15.5 mV , and (f) -58 mV . (g) Azimuthally averaged line cuts of QPI patterns. q is the measured relative distance to the reciprocal lattices $\mathbf{G} = (\pm 2\pi/a_{\text{Se}}, 0)$, $(0, \pm 2\pi/a_{\text{Se}})$, and $(\pm 2\pi/a_{\text{Se}}, \pm 2\pi/a_{\text{Se}})$. The solid line shows Lorentzian fitting peaks with error bars indicated by the peak width. The dashed line in the bottom panel shows the background. (h) Band dispersion obtained from red circles of the QPI patterns overlapped on the ARPES image. The dashed curve shows the superconducting gap from Fig. 3.

that the C_4 symmetry is also broken nonlocally in the 1-UC FeSe/STO- $(\sqrt{13} \times \sqrt{13})$.

IV. DISCUSSION

First, we discuss the local influence of STO-induced electron doping to the 1-UC FeSe film [9,18]. The difference in Δ between atoms 2 and 4 in Fig. 3 shows that the Cooper pair coupling strength varies locally. In general, Δ should be spatially invariant as long as the coherent length is large. However, in the 1-UC FeSe/STO, this can be small as shown above. In fact, from our ARPES data of Fig. 4(h), we estimated the Fermi velocity $v_F \approx (1.4 \pm 0.5) \times 10^5 \text{ m/s}$, and this leads to an extremely short Pippard coherence length of $\xi_0 = \hbar v_F / \pi \Delta \approx (2.1 \pm 0.8) \text{ nm}$, in the same order of magnitude as the unit cell size (1.4 nm). Although a detailed atomic structure model of the STO $\sqrt{13} \times \sqrt{13}$ surface is needed for a precise description, the arrangement of O vacancies and Ti atoms can change the local electron doping and thus lead to a spatial variation in Δ . This situation is similar to that of cuprates [22]. Note that this local influence also appears outside the superconducting gap in Fig. 3(a).

Next let us comment on the origin of the broken C_4 symmetry. When the electronic structure shows lower symmetry than that of the lattice, we usually think about nematic phases. Such a phase has been indeed observed in bulk FeSe and is said to have a relation with superconductivity [27]. However, the presence of a nematic phase has yet to be reported for 1-UC FeSe/STO. Reference [28] reported a possible smectic phase in 2-UC FeSe/STO which disappears for the 1-UC film. Reference [24] reported a constraint on the nematicity in 1-UC FeSe/STO from STM/STS measurements. Similar to the above two works, we emphasize that the present observation of a C_2 symmetry has nothing to do with nematicity and is

rather induced by the STO substrate. This is evidenced by the fact that this broken symmetry appears only after sufficient annealing that removes the excess Se atoms at the FeSe/STO interface [8]. Furthermore, the z patterns break the C_4 symmetry are arranged in the STO surface $\sqrt{13} \times \sqrt{13}$ periodicity. Our QPI results as well as ARPES data are also not consistent with the nematic phase picture.

From the present result, it is most likely that the STO- $(\sqrt{13} \times \sqrt{13})$ surface itself only has C_2 symmetry. There have been reports on the structure determination of this surface [14,15,19]. Among them, Ref. [19] has indeed shown a stacking model of the FeSe/STO- $(\sqrt{13} \times \sqrt{13})$ surface that may induce C_2 symmetry. It would be interesting to utilize first-principles calculations and simulate STM images and compare with our results to determine the real structure of this system.

V. CONCLUSION

In summary, we performed STM/STS measurements to investigate the superconducting properties of 1-UC FeSe/STO- $(\sqrt{13} \times \sqrt{13})$. We found evidence that the superconducting gap size varies locally in the $\sqrt{13} \times \sqrt{13}$ unit cell due to the combination of local electron doping inhomogeneity and short coherence length. Atomic-resolved topographic images, local tunneling dI/dV spectra, and QPI patterns all suggest a substrate-induced broken C_4 symmetry of the 1-UC FeSe.

ACKNOWLEDGMENTS

This work has been supported by Grants-In-Aid from Japan Society for the Promotion of Science (No. 18H03877), the Murata Science Foundation (No. H30-084), the Asahi Glass

Foundation, the Iketani Science and Technology Foundation (0321083-A), Tokyo Tech Challenging Research Award,

Yoshinori Ohsumi Fund for Fundamental Research, and Support for Tokyo Tech Advanced Researchers (STAR).

- [1] J.-F. Ge, Z.-L. Liu, C. Liu, C.-L. Gao, D. Qian, Q.-K. Xue, Y. Liu, and J.-F. Jia, *Nat. Mater.* **14**, 285 (2015).
- [2] Q.-Y. Wang, Z. Li, W.-H. Zhang, Z.-C. Zhang, J.-S. Zhang, W. Li, H. Ding, Y.-B. Ou, P. Deng, K. Chang, J. Wen, C.-L. Song, K. He, J.-F. Jia, S.-H. Ji, Y.-Y. Wang, L.-L. Wang, X. Chen, X.-C. Ma, and Q.-K. Xue, *Chin. Phys. Lett.* **29**, 037402 (2012).
- [3] A. K. Pedersen, S. Ichinokura, T. Tanaka, R. Shimizu, T. Hitosugi, and T. Hirahara, *Phys. Rev. Lett.* **124**, 227002 (2020).
- [4] F.-C. Hsu, J.-Y. Luo, K.-W. Yeh, T.-K. Chen, T.-W. Huang, P. M. Wu, Y.-C. Lee, Y.-L. Huang, Y.-Y. Chu, D.-C. Yan, and M.-K. Wu, *Proc. Natl. Acad. Sci. USA* **105**, 14262 (2008).
- [5] D. Liu, W. Zhang, D. Mou, J. He, Y.-B. Ou, Q.-Y. Wang, Z. Li, L. Wang, L. Zhao, S. He, Y. Peng, X. Liu, C. Chen, L. Yu, G. Liu, X. Dong, J. Zhang, C. Chen, Z. Xu, J. Hu *et al.*, *Nat. Commun.* **3**, 931 (2012).
- [6] S. He, J. He, W. Zhang, L. Zhao, D. Liu, X. Liu, D. Mou, Y.-B. Ou, Q.-Y. Wang, Z. Li, L. Wang, Y. Peng, Y. Liu, C. Chen, L. Yu, G. Liu, X. Dong, J. Zhang, C. Chen, Z. Xu *et al.*, *Nat. Mater.* **12**, 605 (2013).
- [7] C. Tang, D. Zhang, Y. Zang, C. Liu, G. Zhou, Z. Li, C. Zheng, X. Hu, C. Song, S. Ji, K. He, X. Chen, L. Wang, X. Ma, and Q.-K. Xue, *Phys. Rev. B* **92**, 180507(R) (2015).
- [8] F. Li, Q. Zhang, C. Tang, C. Liu, J. Shi, C. Nie, G. Zhou, Z. Li, W. Zhang, C.-L. Song, K. He, S. Ji, S. Zhang, L. Gu, L. Wang, X.-C. Ma, and Q.-K. Xue, *2D Mater.* **3**, 024002 (2016).
- [9] J. Guan, J. Liu, B. Liu, X. Huang, Q. Zhu, X. Zhu, J. Sun, S. Meng, W. Wang, and J. Guo, *Phys. Rev. B* **95**, 205405 (2017).
- [10] J. J. Lee, F. T. Schmitt, R. G. Moore, S. Johnston, Y. T. Cui, W. Li, M. Yi, Z. K. Liu, M. Hashimoto, Y. Zhang, D. H. Lu, T. P. Devereaux, D. H. Lee, and Z. X. Shen, *Nature (London)* **515**, 245 (2014).
- [11] L. Rademaker, Y. Wang, T. Berlijn, and S. Johnston, *New J. Phys.* **18**, 022001 (2016).
- [12] Y. Zhang, J. J. Lee, R. G. Moore, W. Li, M. Yi, M. Hashimoto, D. H. Lu, T. P. Devereaux, D. H. Lee, and Z. X. Shen, *Phys. Rev. Lett.* **117**, 117001 (2016).
- [13] J. Jandke, F. Yang, P. Hlobil, T. Engelhardt, D. Rau, K. Zakeri, C. Gao, J. Schmalian, and W. Wulfhchel, *Phys. Rev. B* **100**, 020503(R) (2019).
- [14] K. Zou, S. Mandal, S. D. Albright, R. Peng, Y. Pu, D. Kumah, C. Lau, G. H. Simon, O. E. Dagdeviren, X. He, I. Božović, U. D. Schwarz, E. I. Altman, D. Feng, F. J. Walker, S. Ismail-Beigi, and C. H. Ahn, *Phys. Rev. B* **93**, 180506(R) (2016).
- [15] D. M. Kienzle, A. E. Becerra-Toledo, and L. D. Marks, *Phys. Rev. Lett.* **106**, 176102 (2011).
- [16] J. Bang, Z. Li, Y. Y. Sun, A. Samanta, Y. Y. Zhang, W. Zhang, L. Wang, X. Chen, X. Ma, Q. K. Xue, and S. B. Zhang, *Phys. Rev. B* **87**, 220503(R) (2013).
- [17] T. Tanaka, K. Akiyama, R. Yoshino, and T. Hirahara, *Phys. Rev. B* **98**, 121410(R) (2018).
- [18] T. Tanaka, K. Akiyama, S. Ichinokura, R. Shimizu, T. Hitosugi, and T. Hirahara, *Phys. Rev. B* **101**, 205421 (2020).
- [19] R. Peng, K. Zou, M. G. Han, S. D. Albright, H. Hong, C. Lau, H. C. Xu, Y. Zhu, F. J. Walker, and C. H. Ahn, *Sci. Adv.* **6**, eaay4517 (2020).
- [20] S. Zhang, T. Wei, J. Guan, Q. Zhu, W. Qin, W. Wang, J. Zhang, E. W. Plummer, X. Zhu, Z. Zhang, and J. Guo, *Phys. Rev. Lett.* **122**, 066802 (2019).
- [21] H. Ding, Y.-F. Lv, K. Zhao, W.-L. Wang, L. Wang, C.-L. Song, X. Chen, X.-C. Ma, and Q.-K. Xue, *Phys. Rev. Lett.* **117**, 067001 (2016).
- [22] C. Howald, P. Fournier, and A. Kapitulnik, *Phys. Rev. B* **64**, 100504(R) (2001).
- [23] The smaller peaks at higher energy are likely due to the nonlinearity of the background.
- [24] D. Huang, T. A. Webb, S. Fang, C.-L. Song, C.-Z. Chang, J. S. Moodera, E. Kaxiras, and J. E. Hoffman, *Phys. Rev. B* **93**, 125129 (2016).
- [25] Note that this feature has been reported also in Ref. [24]. We are not sure about the actual mechanism since the intensity weakening shown by the blue circles in Figs. 4(c)–4(f) cannot be explained by changes in the scattering amplitude of the intra- or interband scattering without assuming some unknown degree of freedom.
- [26] D. Huang, C.-L. Song, T. A. Webb, S. Fang, C.-Z. Chang, J. S. Moodera, E. Kaxiras, and J. E. Hoffman, *Phys. Rev. Lett.* **115**, 017002 (2015).
- [27] T. Shibauchi, T. Hanaguri, and Y. Matsuda, *J. Phys. Soc. Jpn.* **89**, 102002 (2020).
- [28] Y. Yuan, X. Fan, X. Wang, K. He, Y. Zhang, Q.-K. Xue, and W. Li, *Nat. Commun.* **12**, 2196 (2021).